



Cite this: *Soft Matter*, 2016,
12, 3919

Persulfate initiated ultra-low cross-linked poly(*N*-isopropylacrylamide) microgels possess an unusual inverted cross-linking structure†

O. L. J. Virtanen,^{*a} A. Mourran,^b P. T. Pinard^c and W. Richtering^a

Cross-linking density and distribution are decisive for the mechanical and other properties of stimuli-sensitive poly(*N*-isopropylacrylamide) microgels. Here we investigate the structure of ultra-low cross-linked microgels by static light scattering and scanning force microscopy, and show that they have an inverted cross-linking structure with respect to conventional microgels, contrary to what has been assumed previously. The conventional microgels have the largest polymer volume fraction in the core from where the particle density decays radially outwards, whereas ultra-low cross-linked particles have the highest polymer volume fraction close to the surface. On a solid substrate these particles form buckled shapes at high surface coverage, as shown by scanning force micrographs. The special structure of ultra-low cross-linked microgels is attributed to cross-linking of the particle surface, which is exposed to hydrogen abstraction by radicals generated from persulfate initiators during and after polymerization. The particle core, which is less accessible to the diffusion of radicals, has consequently a lower polymer volume fraction in the swollen state. By systematic variation of the cross-linker concentration it is shown that the cross-linking contribution from peroxide under typical synthesis conditions is weaker than that from the use of 1 mol% *N,N'*-methylenebisacrylamide. Soft deformable hydrogel particles are of interest because they emulate biological tissues, and understanding the underlying synthesis principle enables tailoring the microgel structure for biomimetic applications. Deformability of microgels is usually controlled by the amount of added cross-linker; here we however highlight an alternative approach through structural softness.

Received 18th January 2016,
Accepted 8th March 2016

DOI: 10.1039/c6sm00140h

www.rsc.org/softmatter

1 Introduction

Stimuli-sensitive poly(*N*-isopropylacrylamide) (PNIPAM) microgels^{1,2} and derivatives are spherical cross-linked gel particles with radii from tens of nanometers to a few microns. They have found various applications *e.g.* as temperature sensitive microgel coatings^{3–6} that enable easy cell harvesting from cell culture substrates,^{7,8} microlenses,⁹ and stabilizers for smart emulsions.^{10–15} In addition, they have potential biomedical uses.¹⁶

A recent development in this field are hollow microgel particles,^{17–19} which show significantly higher deformability and spreading at interfaces²⁰ in comparison to conventional PNIPAM microgels. Ultra-low cross-linked (ULC) microgel particles^{21,22} exhibit similar properties; therefore both of these

particle types might prove to be useful in biomimetic²³ and loading and release^{24–26} applications.

Excessive deformability of hollow microgels arises from their unconventional structure.¹⁸ Therefore the polymer volume fraction (cross-linking) distribution inside the PNIPAM particles determines their mechanical properties and is an important factor for their permeability to guest molecules, such as enzymes.^{27,28} In the case of ultra-low cross-linked microgels, it has been suggested that these particles possess a similar structure to conventional microgels,²⁹ only with significantly lower cross-linking density.²² In previous work ULC microgels were characterized on a solid substrate, where extensive deformation of the particles has been reported.^{3–5,30–34} In this contribution we investigate dispersion of particles in the swollen state, which leads to a different conclusion: ultra-low cross-linked microgels have an inverted density profile in contrast to conventional fuzzy microgels, *i.e.*, the highest polymer volume fraction is located close to the surface of the particle from where the density decays towards the core.

This unexpected structure can be attributed to hydrogen abstraction and subsequent cross-linking at the particle surface

^a Institute of Physical Chemistry, RWTH Aachen University, Landoltweg 2, 52064 Aachen, Germany. E-mail: otto.virtanen@rwth-aachen.de

^b DWI – Leibnitz Institute for Interactive Materials, RWTH Aachen University, Forckenbeckstr. 50, 52056 Aachen, Germany

^c Central Facility for Electron Microscopy, RWTH Aachen University, Ahornstr. 55, 52074 Aachen, Germany

† Electronic supplementary information (ESI) available. See DOI: 10.1039/c6sm00140h

by persulfate initiator radicals^{35,36} during the late stages of the polymerization. To test this hypothesis, we first incubate non-cross-linked PNIPAM particles in potassium persulfate (KPS) solutions and show that the hydrogen abstraction effect is strong enough to create stable gel particles with an inverted structure. In contrast the non-cross-linked particles dissolve to the continuous phase upon cooling below PNIPAM volume phase transition temperature (VPTT). We then compare batches initiated with KPS and a redox initiation system, which does not cross-link the particles, and show that under typical reaction conditions the cross-linking extent by KPS is comparable to less than 1 mol% *N,N'*-methylenebisacrylamide (BIS) in the batch. Conditions leading to different microgel architectures are schematically depicted in Fig. 1.

An accurate characterization of the particle structure enables one to establish detailed structure–property relationships and

ultimately control the synthesis of PNIPAM microgels for the application at hand. A suitable method for structure characterization of microgels of this particle size range in the non-disturbed state in dispersion is static light scattering. Typically a model expression for the scattered intensity is required to obtain quantitative structure data of the scatterers, but here we used a more general direct inversion method, which yields the radial density profile for spherical particles. This method is briefly introduced in the next section and is useful for classifying particles whose structure is not known *a priori*. The following sections discuss the extent of persulfate cross-linking, and are of interest for practitioners involved in synthesis and application of microgels. The light scattering experiments are supplemented by analyzing the topography of the dried microgels on a solid support.

2 Model expression for scattered light intensity

Light scattering from particles that are small in comparison to the wavelength of the incident laser radiation or have a small refractive index difference to the surrounding solvent can be described by Rayleigh–Debye–Gans (RDG) theory (Chapter 8 by Glatter in ref. 37). Large microgel particles described in this work do not fulfill the first condition, but due to being extensively swollen with solvent the overall refractive index of these particles is close to the refractive index of the solvent. Therefore it is unnecessary to account for Mie scattering effects that are observed for large particles with a high refractive index mismatch with respect to the matrix. For further discussion regarding the possible Mie effects, see ESI.†

In the RDG regime the average scattered light intensity from a dispersion of spherical particles with number density n and particle radius distribution function $D(R)$ at scattering vector magnitude q is given by ref. 29 and 38

$$I(q) = n\Delta\rho^2 \int_0^\infty D(R)V(R)^2 P(q, R)dR \quad (1)$$

Here $V(R)$ and $P(q, R)$ denote the scattering mass and the form factor of a particle with radius R , respectively. $\Delta\rho$ is the scattering contrast, which, in our case, is proportional to the difference between the refractive indices of the solvent swollen particles and the continuous phase. The form factor $P(q, R)$, square of the scattering amplitude F , is given by

$$P(q, R) = F^2 = \left[\frac{b(q, R)}{b(0, R)} \right]^2 \quad (2)$$

where $b(q, R)$ is the scattering length of a particle with radius R . For particles with spherical symmetry, the scattering length depends on the radial excess contrast function $\alpha(r)$.

$$b(q, R) = 4\pi \int_0^R r^2 \alpha(r) \frac{\sin qr}{qr} dr \quad (3)$$

For particles made only of PNIPAM, $\alpha(r)$ is proportional to the density (volume fraction) of the polymeric material inside the particle at radial coordinate r .

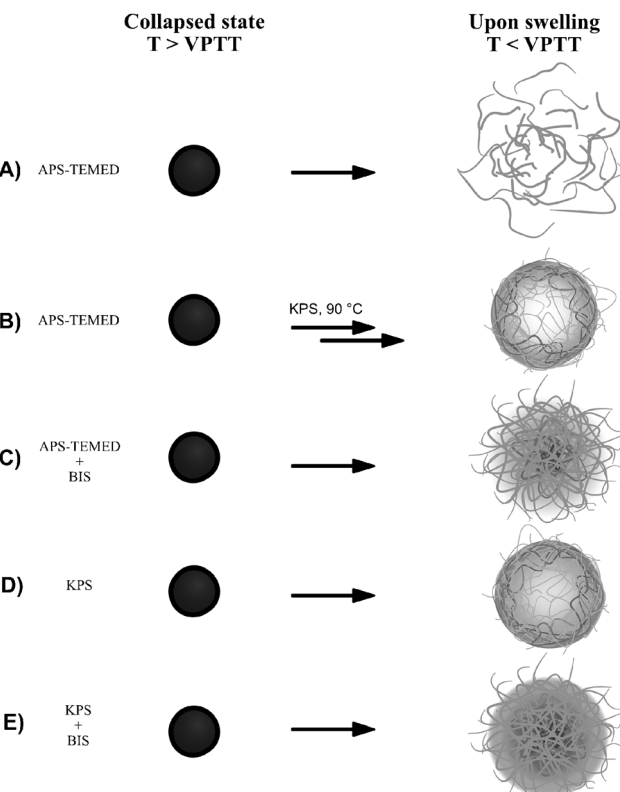


Fig. 1 The effect of the initiator system and the presence of the cross-linker on the microgel architecture. Regardless of the initiation method and the cross-linker, PNIPAM polymer particles are always homogeneous spheres in the collapsed state at the end of the polymerization. Upon cooling and swelling different structures are realized due to different cross-linking mechanisms: (A) APS-TEMED initiated particles without the cross-linker break to fragments, (B) APS-TEMED initiated particles that are transferred and incubated in hot aqueous KPS solution after the polymerization exhibit an inverted microgel structure due to persulfate cross-linking of the surface, (C) APS-TEMED initiated particles polymerized with the cross-linker BIS exhibit a fuzzy sphere structure, (D) KPS initiated particles without the cross-linker have an inverted structure analogous to (B) and (E) KPS initiated particles with cross-linker BIS show a fuzzy structure but with higher surface cross-linking density due to persulfate cross-linking.

Discretizing the unknown excess refractive index difference profile function $\alpha(r)$ in eqn (3) to s steps, evaluating the integral and inserting in eqn (2) result in the form factor for a particle with s concentric shells³⁸

$$P_s(q, R, \vec{\alpha}) = \frac{1}{V^2} \left[\alpha_1 V_1(R) F_1(q, R) + \sum_{i=2}^s (\alpha_i - \alpha_{i-1}) V_i(r_i) F_i(q, r_i) \right]^2 \quad (4)$$

with V_i , F_i and V given by

$$V_i(r_i) = \frac{4}{3} \pi r_i^3 \quad (5)$$

$$F_i(q, r_i) = \frac{3}{(qr_i)^3} [\sin(qr_i) - qr_i \cos(qr_i)] \quad (6)$$

$$V = \alpha_1 V_1(R) + \sum_{i=2}^s \alpha_i V_i(r_i) \quad (7)$$

Here i refers to the i th concentric shell, with the 1st shell being the outermost. V is the total scattering mass of the particle, V_i and F_i are the scattering mass and the scattering amplitude of a homogeneous sphere with radius r_i , respectively, and α_i are the components of the radial excess contrast vector for each shell.

The absolute refractive index profile and the number of particles n are not of primary interest for us in this work. Therefore $\Delta\rho(r)^2$ and n are combined to a scaling parameter A , so that eqn (1) becomes

$$I_s(q, A, \vec{\alpha}) = A \frac{\int_0^\infty D(R) V(R)^2 P_s(q, R, \vec{\alpha}) dR}{\int_0^\infty D(R) V(R)^2 dR} \quad (8)$$

A small intensity fraction η of the incident beam is reflected back from the inside wall of the cuvette, which leads to a scattering process in the opposing direction to the incident beam. Accounting for this phenomenon leads to the model expression for the total scattered intensity

$$I^M(q, A, \eta, \vec{\alpha}) = I_s(q, A, \vec{\alpha}) + \eta I_s(q', A, \vec{\alpha}) \quad (9)$$

where q' is the scattering vector magnitude of the back reflected beam observed at q , given by

$$q' = \frac{4\pi n}{\lambda_0} \sin\left(\frac{\pi - \theta}{2}\right) \quad (10)$$

Here n is the refractive index of the dispersion, λ_0 is the wavelength of the incident radiation in a vacuum and θ is the scattering angle where the detector is positioned. For the particle radius distribution function $D(R)$ we use Burr Type XII distribution

$$D(R, \vec{d}) = D(R, S, B, C) = \frac{BC}{S} \left(\frac{R}{S}\right)^{B-1} \left[1 + \left(\frac{R}{S}\right)^B\right]^{-C-1} \quad (11)$$

where the parameter vector \vec{d} contains parameters S , B and C relating to the scale of the distribution, its width and skewness, respectively. This flexible distribution enables both symmetric and tailed particle size distributions. In prior work²⁹ the Gaussian function has been used for the radius distribution function.

Further discussion on its applicability for the particles used in this work can be found in the ESI.[†]

The density profile and the particle size distribution parameters are evaluated by minimizing the regularized chi-squared with respect to total parameter vector \vec{p}

$$\chi_{\text{reg}}^2(\vec{q}, \vec{p}, \lambda) = \sum_{j=1}^M \sum_{i=1}^N \left(\frac{I_j^E(q_{ji}) - I_j^M(q_{ji}, A_j, \vec{\alpha}, \vec{d})}{\sigma_{ji}} \right)^2 + \lambda^2 \|L_1 \vec{\alpha}\|_1 \quad (12)$$

with

$$\vec{p} = [A_1 \dots A_M \ \eta_1 \dots \eta_M \ \vec{\alpha} \ \vec{d}] \quad (13)$$

The M datasets recorded at different wavelengths, each consisting of N measurement points $I^E(q_i)$ with experimental uncertainty σ_i , are fitted globally. That is, all the model parameters are shared between the datasets except the scaling and backreflection magnitude parameters.

Finding $\vec{\alpha}(r)$ from eqn (12) is an ill-conditioned problem, *i.e.*, the solution is very sensitive to the unavoidable noise in the data and even rounding errors resulting from finite precision arithmetic. In order to obtain physically meaningful approximations to $\vec{\alpha}(r)$, we use Tikhonov regularization with total variation smoothing norm (the last term) in eqn (12). Regularization parameter λ determines the smoothness of the solution, L_1 is the discrete first derivative operator, and $\|\cdot\|_1$ stands for the vector 1-norm. When justified, also second derivative smoothing norm $\lambda^2 \|L_2 \vec{\alpha}\|_2$ can be used. Here L_2 is the discrete second derivative operator and $\|\cdot\|_2$ refers to vector 2-norm. A good introduction to discrete inverse problems and regularization was provided by Hansen.³⁹

A reasonable value for λ can be evaluated by the so-called *L*-curve criterion. In this approach, the quality of the fit is evaluated against the regularity of the solution, *i.e.*, the solution is calculated with multiple λ values and the solution norm $\|\vec{\alpha}\|_2$ is plotted against the residual norm of the solution $\|I^M - I^E\|_2$. The curve forms typically an *L*-shape and a suitable λ value is found at the corner of the curve. This specific solution is usually a good compromise between fitting the data and the regularity of the solution, *i.e.*, not fitting the noise.

The direct inversion method described here is not as general as the indirect transformation methods first described by Glatter⁴⁰ and later *e.g.* Svergun,⁴¹ which yield the pair distance distribution function, and require an additional deconvolution step^{42,43} to obtain the radial profile for spherical particles. The advantage of our procedure however is that it works in our existing software framework, MATLAB program FitIt![‡] and is customizable to our specific requirements. For the program's ability to resolve different particle structures in the presence of noise and systematic distortions typical of static light scattering measurements, the interested reader is referred to performance evaluation by test cases in the ESI.[†]

[‡] Available from the author or www.github.com/ovirtanen/fitit.

3 Experimental

3.1 Particle synthesis

Non-stirred precipitation polymerization^{44,45} was used to synthesize all the particles. This is a rapid highly reproducible small-scale synthesis method, which yields microgels with narrow size distribution. For KPS initiated batches master solutions of NIPAM, BIS and KPS were prepared. The master solutions were diluted and mixed in a way that 5 samples with varying BIS concentration (0, 0.4, 0.8, 2.0, 3.5 and 5.1 mol%) but constant NIPAM (7.1×10^{-2} mol dm⁻³) and KPS (3.1×10^{-3} mol dm⁻³) concentrations were obtained. One milliliter of reaction mixtures were transported to five test tubes with 10 mm diameter and sealed with rubber septa. All the five tubes were purged with nitrogen for 30 minutes and then immersed into an oil bath tempered at 60 °C. The tubes were let to react overnight and transferred to an oven without letting them cool down below PNIPAM VPTT. APS-TEMED initiated batches were prepared similarly, but APS solutions were held separate from the NIPAM-BIS-TEMED solutions. After immersion to the oil bath, 0.5 ml of deoxygenated APS solution was injected to 0.5 ml monomer-TEMED solution using 1 ml syringes in order to initiate the polymerization. The end concentrations of NIPAM, APS and TEMED were 1.5×10^{-1} , 3.1×10^{-3} and 4.7×10^{-3} mol dm⁻³, respectively. BIS concentrations for APS-TEMED batches were 0.4, 0.8, 1.9, 3.0, 4.1 and 5.1 mol%. NIPAM concentration was doubled to compensate for the faster initiation rate with the APS-TEMED system. BIS mole percentages were kept the same, except 0 mol% BIS was replaced with 0.4 mol%. After taking samples for DLS analysis, the samples were ultracentrifuged for 1 h at 30 000 rpm three times to remove any unreacted monomer and non-attached polymer.

3.2 Dynamic light scattering

All the particles were analyzed in the collapsed state at 50 °C without letting them cool down below PNIPAM VPTT between synthesis and characterization. Particle dispersions were diluted by hot double distilled water to avoid multiple scattering. For DLS measurements, a 3D-DLS goniometer with one beam blocked $\lambda = 633$ nm was used. Typically 25 correlograms were acquired from 45 deg to 120 deg with the minimum acquisition time of 90 s. 2nd order cumulant expansion was fitted to the electric field correlation functions and the mean diffusion coefficient was solved by linear fit to

$$\Gamma_2 = Dq^2 \quad (14)$$

Here Γ_2 is the mean decay rate of the correlation function from the 2nd order cumulant fit, D is the mean diffusion coefficient and q is the magnitude of the scattering vector. The hydrodynamic volume was calculated from the Stokes-Einstein relation and the hydrodynamic volume by assuming the particles to be spheres with the radius of the hydrodynamic radius.

3.3 Static light scattering

Three sealed construction goniometers were used to measure form factors, all supplied by SLS-Systemtechnik GmbH. FICA and

SOFICA type goniometers were equipped with diode lasers with wavelengths of 658 nm (15° to 146°, 1° increments) and 405 nm (25° to 145°, 1° increments), respectively. A new SLS Type 3 goniometer, which has improved optics and electronics, accommodates three lasers that can be rotated to change the measurement wavelength. Wavelengths of 404 nm and 642 nm (15° to 155°, 1° increments) were used. All the samples were diluted from the purified dispersions and measured in 20 mm diameter cuvettes at 20 °C in water. Solvent trace was subtracted from all the measurements. Minimum two datasets with different wavelengths were acquired from each batch. Typically different concentrations for blue and red lasers were used to avoid multiple scattering in the blue laser measurements. The scattering traces were imported to program FitIt! and inverted using 20 point discretization. The regularization parameter was determined from the *L*-curve, which was calculated for each batch.

3.4 Scanning force microscopy

The microgels were measured on a hydrophilic silicon wafer (cleaned by ultrasonication in isopropanol, dried, and treated with UV/O₂ for 12 min). Typically 200 µl of purified microgel dispersion was deposited on the silicon wafer surface and the wafer was rotated at a speed of 3000 rpm for 4 minutes to spread the particles on the surface. Surface coverage was varied by diluting the master dispersion. Scanning force microscopy (AFM) images were recorded on a Nanoscope V (Bruker) instrument in tapping mode. Cantilevers with resonance frequencies of 250–300 kHz and spring constants around 42 N m⁻¹ were used. NanoScope Analysis v.1.50 software (Bruker) was used to analyze the AFM micrographs.

3.5 Scanning electron microscopy

Images were acquired using a scanning electron microscope, JEOL JXA8530F, to visually determine the size distribution of the macromolecules. The solutions were dried on GaAs wafer and observed using an accelerating voltage of 15 kV and an approximate beam current of 5 nA. The magnification was varied between 5000 and 7000. A image analysis routine written in Python using the *scipy*⁴⁶ and *scikit-image*⁴⁷ libraries was developed to identify every macromolecule while minimizing artifacts such as agglomerated molecules or surface debris. After median filtering to remove image noise, images were converted to binary images using the Otsu algorithm. Molecules with an area less than 1 µm², with a circularity ($4(\text{area})/(\pi(\text{max. diameter})^2)$) less than 0.75 and with a sphericity ($4\pi(\text{area})/(\text{perimeter})^2$) less than 0.5 were discarded.

4 Results and discussion

4.1 KPS induces cross-links to the particle periphery leading to a core depleted particle structure

To demonstrate the cross-linking capability of the KPS initiator, non-cross-linked PNIPAM particles were prepared using the APS-TEMED redox initiation system. The resulting batch was kept hot and divided into hot aqueous KPS solutions under an

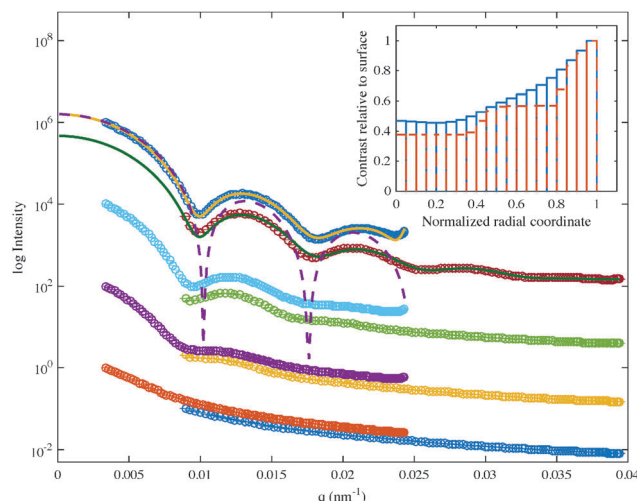


Fig. 2 Form factors of initially non-cross-linked PNIPAM particles incubated in KPS solutions, in the swollen state at 20 °C in water. Intensities are scaled arbitrarily for clear presentation. KPS concentrations from top down: 3.12×10^{-3} , 1.57×10^{-3} , 7.78×10^{-4} and 0 mol dm⁻³. In each sample the low q range was measured with a wavelength of 658 nm and the high q range with 405 nm. The solid lines are the global fit on the particles formed at the highest KPS concentration calculated using 2nd derivative smoothing norm. The dashed line is the reference form factor of a monodisperse hard sphere with the same mean square radius of gyration as the KPS cross-linked particles. The inset shows solutions to the density profile of the particles normalized to the shell contrast. The solid line is the solution with $\log \lambda = 2.8$ using second derivative smoothing norm, and the dashed line with $\log \lambda = 2.5$ using total variation smoothing norm.

argon atmosphere without letting the particles cool down below PNIPAM VPTT in between. Hot water was used as a reference. Fig. 2 shows the form factors of the particles measured in the swollen state at 20 °C after 3.5 h of incubation in the collapsed state at 90 °C.

The lowest featureless form factor in Fig. 2 shows that particles incubated in hot water redisperse to fragments of various sizes upon swelling below PNIPAM VPTT (Fig. 1 case A). In contrast to the particles which only suffered the hot water treatment, KPS incubated particles exhibit signs of cross-linking. With increasing KPS concentration, forward scattering intensifies indicating the increasing molecular weight of the scatterers, and oscillations characteristic of spherical particles emerge.

Given that the surface of the collapsed particles is the most exposed to the hydrogen abstraction of the KPS radicals, one expects the cross-linking density, and the polymer volume fraction, to be the highest at the periphery of the KPS cross-linked microgels. This assumption is supported by comparison of the experimental data to a scattering pattern of a homogeneous sphere with the same mean square radius of gyration as the KPS incubated particles. As can be seen in Fig. 2, the first maximum of the experimental data protrudes to higher intensity than that of the homogeneous reference particle. This behavior is characteristic of spherical structures that are core depleted, *i.e.*, that are less dense in the core in contrast to the periphery of the particle.

Solutions to the density profile of particles calculated with total variation and 2nd derivative smoothing norms are shown

in the inset of Fig. 2. Both solutions agree with the features already observed in the q space; the polymer volume fraction is the highest at the surface and decays with distance to the core. Total variation smoothing norm characteristically produces a less smooth solution than 2nd derivative smoothing norm; we however assume the latter to be a better approximation to the real density profile as there is no reason to expect a discontinuous particle structure.

It is reasonable to expect that the diffusion of the radicals to the core of the dense collapsed polymer particles becomes increasingly difficult with the radial distance from the surface, and consequently the radicals create more active sites near the surface, which can further react to cross-links. Therefore the cross-linking density decreases continuously with distance towards the core. Upon swelling loosely attached polymer chains (sol fraction) likely diffuse out of the network resulting in a rather sparse structure with an inverted cross-linking distribution in respect to conventional microgels (Fig. 1 case B).

4.2 How strong is the KPS cross-linking effect?

The cross-linking effect of the initiator can be strong enough to exceed the gel point in the particles. The natural question that follows is how does the cross-linking density compare to the explicit use of a cross-linker, such as BIS. Strong additional cross-linking contribution will affect the particle properties such as mechanical strength, swelling ratio and loading and release characteristics, possibly in a detrimental way if not accounted for.

As KPS and BIS create cross-links specifically to the periphery and core of the particle, respectively, the cross-linking efficiency of KPS can be accounted for by synthesizing particles with varying BIS concentration but the same KPS concentration. At the point where both contributions are comparable, one expects the particles to have a rather homogenous structure, *i.e.*, similar to that of a hard sphere. In the absence of initiator induced cross-links, particles initiated with the APS-TEMED system should instead always show a fuzzy microgel structure.

Fig. 3 shows the hydrodynamic volume of KPS and APS-TEMED initiated batches in the collapsed state after the reaction. The particles in the collapsed state are assumed to have a homogeneous structure and therefore the volume in the collapsed state reflects the mass of the particles. The molecular weight of the particles clearly increases with the amount of BIS, which we earlier attributed to the decrease of particle number density with BIS concentration.⁴⁵ All the KPS initiated batches appear turbid in the swollen state at room temperature (Fig. 4), which confirms that colloidal particles form even when no additional cross-linker is present in the initial monomer mixture.

Fig. 5 shows the scattering data acquired for the KPS initiated batches. The initial visual inspection reveals that all of the samples have narrow particle size distributions, which can be seen from the multiple distinguished minima throughout the q range. For selected samples form factors of homogeneous spheres with the same mean square radius of gyration are plotted for reference. In the case of the 0 mol% BIS sample, which is the limiting case for the ultra-low cross-linked microgels,

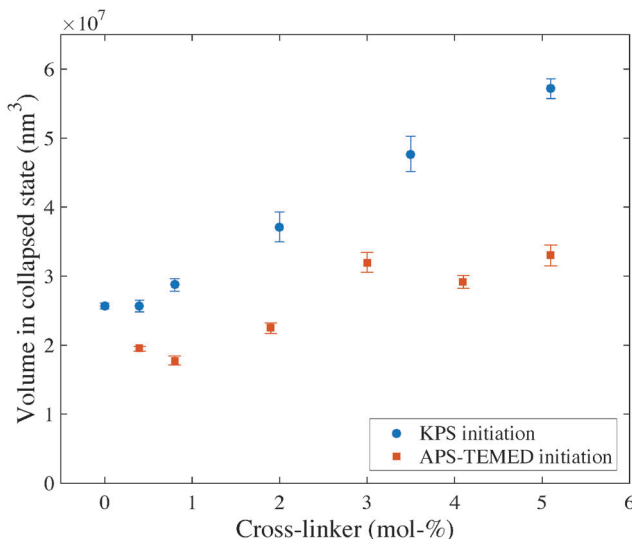


Fig. 3 Hydrodynamic volume of particles initiated by the KPS or APS-TEMED system at 60 °C, and measured in the collapsed state at 50 °C. The particles were not let to cool below VPTT between the synthesis and characterization. NIPAM concentration in each batch was 7.1×10^{-2} mol dm $^{-3}$ for KPS initiated batches and 1.5×10^{-1} mol dm $^{-3}$ for APS-TEMED initiated batches to compensate for the faster initiation rate and the lack of spontaneous cross-linking. KPS concentration was 3.1×10^{-3} mol dm $^{-3}$ and APS and TEMED concentrations were 3.1×10^{-3} mol dm $^{-3}$ and 4.7×10^{-3} mol dm $^{-3}$, respectively.

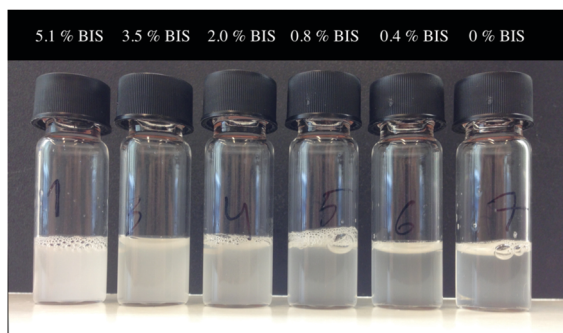


Fig. 4 Microgel dispersions initiated by KPS after purification by centrifugation at room temperature. Turbidity of the dispersions indicates that colloidal particles are present regardless of the amount of cross-linker BIS in the initial reaction mixture.

it can be seen that the first maximum protrudes to higher intensity than that of the homogeneous sphere, which indicates the core depleted, or inverted, structure, similar to externally cross-linked particles. For the samples other than 0 mol% BIS, the form factors decay faster than those of homogeneous spheres, which implies the fuzzy sphere structure.²⁹

The computed solutions for density profiles of the KPS initiated batches are shown in Fig. 6. Detailed discussion of the routine ability to resolve fuzzy structures is included in the ESI.† Briefly, in a (experimentally) limited q range fuzzy structures generate similar scattering patterns as core shell particles, which is reflected in these reconstructions. All the solutions except with higher than 0.8 mol% BIS indicate a low density region on the periphery of

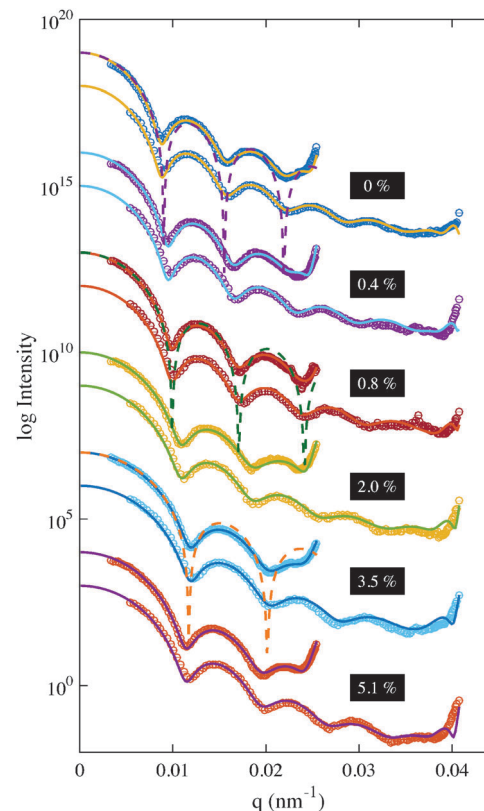


Fig. 5 KPS initiated batches measured at 20 °C in water. From the top down 0, 0.4, 0.8, 2.0, 3.5, and 5.1 mol% BIS. Two datasets per sample were acquired; datasets belonging to the same sample are grouped together. Solid lines are the global fits to data. Dashed lines show form factors of homogeneous spheres with the same mean square radius of gyration as the corresponding particles.

the particles. This is a generally accepted feature of swollen microgels, which arises from the fact that the cross-linker BIS reacts faster than NIPAM, resulting in higher cross-linking density in the core of the particles (Fig. 1 case E). The final structure of the microgels is attained when the non-cross-linked sol fraction of the polymer detaches from the gel fraction upon particle swelling below VPTT. The sol fraction has been shown to approach 50% for *N*-isopropylmethacrylamide particles with 2 mol% BIS,⁴⁸ indicating that the actual gel particles are just rather thin scaffolds in comparison to the mass of the particles in the collapsed state at the end of the polymerization. Stieger *et al.*²⁹ successfully described the resulting swollen, fuzzy particle structure with a radially decaying density profile in their scattering model.

In the absence of an additional cross-linker in the batch, we have no mechanistic reason to expect a radially decaying density profile. In contrast, as we have shown, exposure of polymer particles to initiator radicals induces cross-links to the periphery of the particles. Analogous to KPS incubated initially non-cross-linked particles, 0 mol% BIS particles also exhibit a core depleted structure. Because the microgels synthesized by precipitation polymerization grow from the core outwards, it is reasonable to expect that cross-linker free KPS initiated

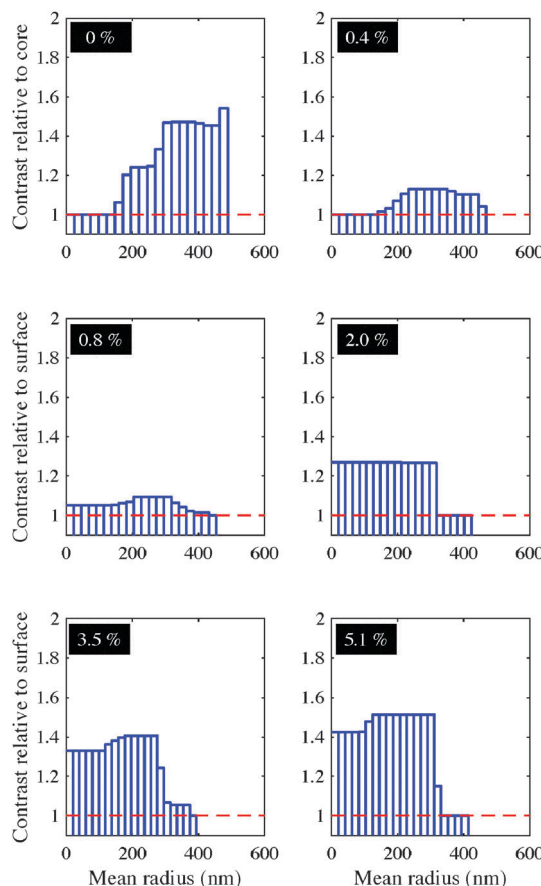


Fig. 6 Solutions to the density profiles for KPS initiated batches calculated using total variation smoothing norm with 20 point discretization.

particles always have a certain amount of cross-links in their core due to transfer reactions during the polymerization (Fig. 1 case D). Given that all the particles in Fig. 5 were synthesized at 60 °C, this experiment shows that initiator cross-linking is a

significant process even at typical synthesis temperatures, in contrast to 90 °C, which was used for incubation.

The inversion routine determines the scattering contrast relative to the outermost layer of the particles. The solutions in Fig. 6 show that the turn over point from inverted (hollowish) to fuzzy takes gradually place between 0 and 2.0 mol% BIS. The particles with 0.8 mol% BIS exhibit a rather homogeneous structure; the difference in the periphery and the core of particles is clearly more pronounced for batches with 2.0 mol% and higher BIS content, indicating a fuzzy microgel structure. Under these reaction conditions the cross-linking contribution from KPS is comparable to the contribution from BIS for the 0.8 mol% BIS batch but diminishes rapidly afterwards when cross-linker concentration is increased.

AFM micrographs of 0, 0.4 and 2.0 mol% BIS batches in Fig. 7 show that at high surface coverage 0 mol% BIS particles deform and buckle, whereas buckling is not seen for 0.4 mol% and higher BIS batches. Buckling was inferred from the non-uniform height profile of the microgel, they exhibit an elevated edge or an ellipsoidal shape deflated in the center. Similar buckled shapes were reported by Bachman *et al.* in their AFM study on ultra-low cross-linked particles.²² Buckling of cross-linker free particles is in line with the static scattering result that indicated the cross-linker free particles having the highest polymer volume fraction (cross-linking density) at the particle surface. As the particle surface is somewhat stiffer and denser in comparison to the particle core, the soft spheres adopt a buckled shape whenever a high particle surface density limits their deformation and spreading.

When this spatial constraint is removed 0 mol% BIS particles demonstrate their high deformability and extensive spreading on the substrate (Fig. 8). In the crowded environment the 0 mol% BIS particles protrude approximately 10 nm from the substrate, whereas on the uncrowded substrate the particles spread over several square micrometers and protrude only 3–7 nm from the substrate. No buckling can be observed under these

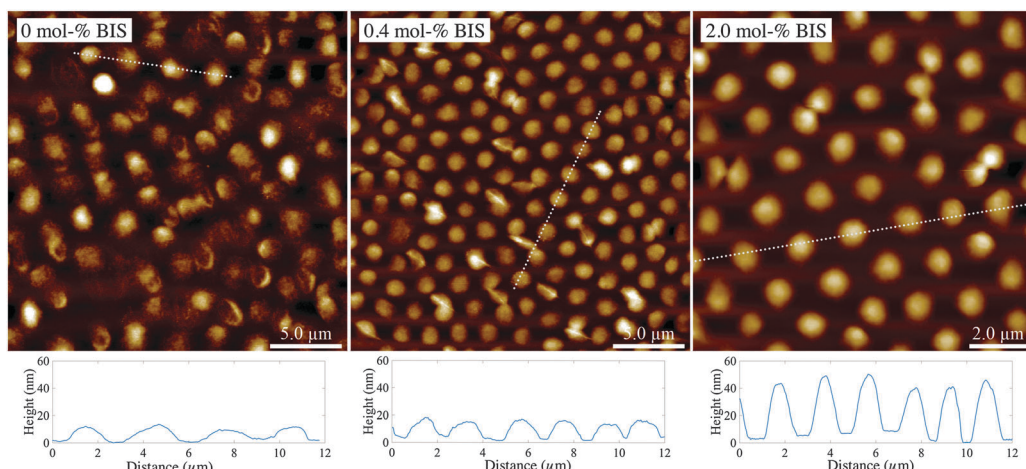


Fig. 7 AFM micrographs and selected cross-sections of KPS initiated 0, 0.4 and 2.0 mol% BIS samples at high surface coverage deposited on the SiO₂ substrate. The height of the particles on the substrate increases with increasing BIS content, indicating that more polymer is retained in the gel fraction at higher cross-linking degrees.

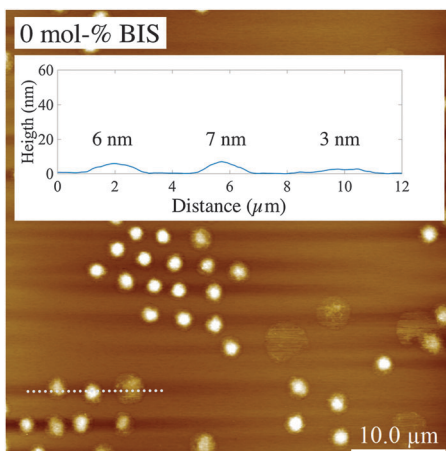


Fig. 8 AFM micrograph of the KPS initiated 0 mol% BIS sample at low surface coverage.

circumstances; however, excessive spreading on the substrate may even cause mechanical failure of the ultrasoft microgels. This is evidenced by the extremely flat, somewhat irregular shapes in Fig. 8. The form factors in Fig. 5 show beyond doubt that 0 mol% BIS particles adopt a spherical shape in dispersion, and their thickness of only 3–7 nm on the substrate indicates that the KPS cross-linked particles possess a thin, vesicle-like geometry in the swollen state. These results contradict the notion of the core-localized cross-linking profile, which has been proposed in the literature.^{22,49}

4.3 All APS-TEMED redox initiated particles exhibit a fuzzy structure

Reference measurements for APS-TEMED initiated batches are shown in Fig. 9 and the solutions to the density profile in Fig. 10. The BIS fractions were kept the same except the 0 mol% BIS KPS batch, which was replaced with 0.4 mol% BIS for obvious reasons. For specific samples the equivalent homogeneous sphere has been plotted; in all the cases the experimental data decay faster than the form factors of homogeneous particles implying fuzzy structures. Reconstructions of the density profiles in Fig. 10 are compatible with the features observed in q space; all solutions indicate the low density periphery typical of fuzzy microgels.

The two low cross-linker concentration batches 0.4 mol% and 0.8 mol% BIS appear to have an extensive low density region in contrast to higher BIS concentration batches. As concluded earlier, at such low BIS contents the cross-linking density resulting from KPS is likely comparable to that of the explicit cross-linker, giving more definition to KPS initiated batches. In the lack of KPS, the low BIS concentration in the batch results in an excessively fuzzy structure.

4.4 Swelling characteristics of the ultra-low cross-linked particles

An important question is whether the high swelling of the ultra-low cross-linked microgels is due to the structure of the

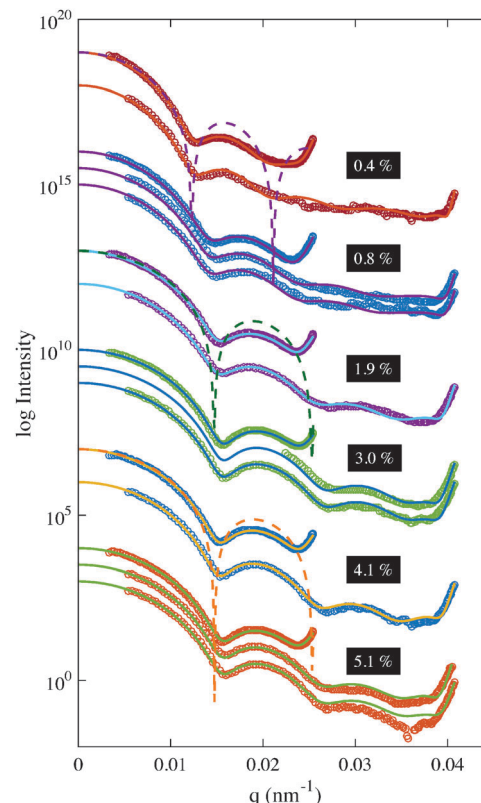


Fig. 9 APS-TEMED initiated batches measured at 20 °C in water. From the top down 0.4, 0.8, 1.9, 3.0, 4.1, and 5.1 mol% BIS. Minimum two datasets per sample were acquired; datasets belonging to the same sample are grouped together. Solid lines are the global fits to data. Dashed lines show form factors of homogeneous spheres with the same mean square radius of gyration as the corresponding particles.

particles, which qualitatively differs for KPS initiated batches depending on the BIS content, or the overall cross-linking density. Comparison of the swelling capability of KPS and APS-TEMED initiated batches, which always have fuzzy sphere architecture regardless of the amount of BIS, is shown in Fig. 11. Interestingly, regardless of the initiation method, the swelling ratio of the microgels remains constant at 6–7 above 2 mol% BIS, but increases rapidly with decreasing BIS content below the 2 mol% threshold. In the interval of 0 to 2 mol% BIS the particle structure of the KPS initiated particles changes from inverted to fuzzy, whereas APS-TEMED initiated particles remain fuzzy. Nevertheless high swelling ratios are observed for both particle types, and therefore this behavior cannot be due to the particle architecture but the overall cross-linking density. For KPS initiated batches the change in the particle architecture was not observed to affect the VPTT behavior (ESI†).

The distinction between particles initiated by initiators that do and do not induce cross-links on the particle periphery should be kept in mind in experimental design. APS-TEMED initiated particles adhere to the conventional notion of PNIPAM microgels. These particles always exhibit a fuzzy sphere structure, where the overall particle density is controlled by the amount of explicit cross-linker in the batch. In contrast, a series of particles initiated by KPS with varying BIS concentration not only have an

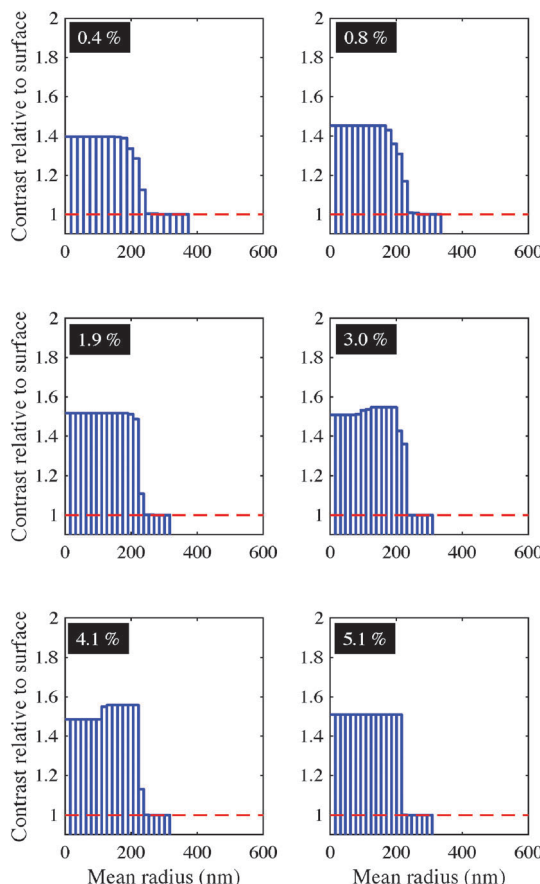


Fig. 10 Solutions to the density profiles for APS-TEMED initiated batches calculated using total variation smoothing norm with 20 point discretization.

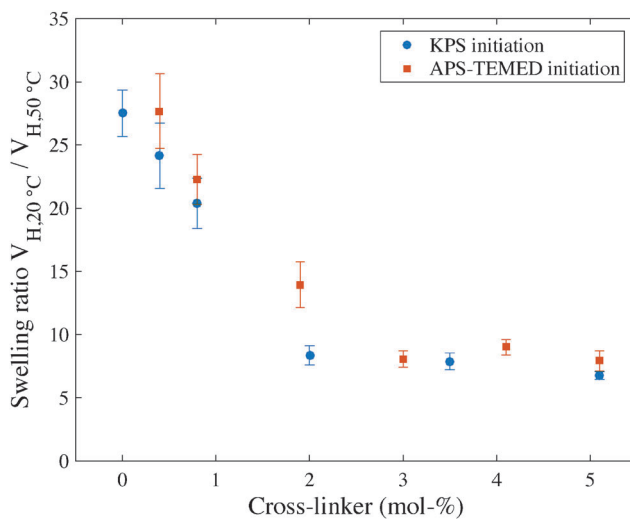


Fig. 11 Swelling ratio ($R_{H,20}^{\circ C}/R_{H,50}^{\circ C}$)³ for purified KPS and APS-TEMED initiated batches with the initial cross-linker content in the reaction mixture.

additional cross-linking contribution from the persulfate initiator, but also change particle architecture at the low BIS end of the spectrum. Persulfate initiated batches (we have also confirmed this effect for ammonium persulfate), start as sparse, inverted,

structures if no cross-linker is used, go through a rather homogeneous structure at the point where persulfate and BIS contributions are comparable, and end up in a fuzzy sphere structure when the cross-linking contribution of BIS is higher than that of the persulfate initiator. These considerations are important for studies that investigate microgel properties as a function of cross-linker content⁵⁰ in order to avoid misinterpretation of data.

5 Conclusions

In this contribution we investigated the structure of ultra-low cross-linked, deformable PNIPAM microgels, which are synthesized by cross-linker free precipitation polymerization. Static light scattering data showed that these particles possess an inverted polymer volume fraction profile in contrast to conventional microgels, *i.e.*, polymer density in the particles was the highest close to the particle surface and decayed radially towards the core. SFM micrographs of the same particles revealed buckled shapes at high surface coverage, which supports the idea of an ultra-soft microgel consisting of a thin shell. This result contradicts the earlier notion according to which cross-linker free synthesis results in a weakly cross-linked conventional microgel particle structure. Incubation of non-cross-linked PNIPAM particles in aqueous KPS solutions at elevated temperatures showed that the core-depleted structure can be attributed to the hydrogen abstraction induced surface cross-linking by the KPS radicals at the late stages of the reaction. Increasing the cross-linker content gradually showed that the crosslink density from the initiator cross-linking corresponded to the use of less than 1 mol% BIS in our specific case. Under typical polymerization conditions one should be aware that synthesis below 1 mol% threshold can lead to an untypical particle structure, and can have consequences regarding the intended application of the particles as many properties of microgels are determined by the cross-linking distribution.

Understanding the structure of cross-linker free PNIPAM microgels may open the way for further applications. Hollow microgel particles^{17–19} have attracted interest due to their high deformability at interfaces²⁰ and possible transport properties. Ultra-low cross-linked particles might share some of the properties of the hollow particles, with the benefit of being easy to synthesize in a simple batch process. As we have shown, it is also possible to synthesize non-cross-linked monodisperse PNIPAM particles, which dissolve to the solution upon cooling below PNIPAM VPTT. A straightforward step further would be to use these particles as scaffolds for hollow microgels in a two step batch process. Typically inorganic cores, which require harsh and cumbersome removal processes, are used for this purpose.

Acknowledgements

Virtanen thanks Prof. O. Glatter for discussions regarding the Mie effect and form factor inversion. Sonderforschungsbereich 985 Functional Microgels and Microgel Systems of Deutsche Forschungsgemeinschaft is acknowledged for financial support.

References

- 1 R. H. Pelton and P. Chibante, *Colloids Surf.*, 1986, **20**, 247–256.
- 2 R. Pelton, *Adv. Colloid Interface Sci.*, 2000, **85**, 1–33.
- 3 S. Schmidt, H. Motschmann, T. Hellweg and R. von Klitzing, *Polymer*, 2008, **49**, 749–756.
- 4 C. D. Sorrell and L. A. Lyon, *Langmuir*, 2008, **24**, 7216–7222.
- 5 A. Burmistrova and R. von Klitzing, *J. Mater. Chem.*, 2010, **20**, 3502–3506.
- 6 A. Burmistrova, R. Steitz and R. von Klitzing, *Chem.-PhysChem*, 2010, **11**, 3571–3579.
- 7 S. Schmidt, M. Zeiser, T. Hellweg, C. Duschl, A. Fery and H. Möhwald, *Adv. Funct. Mater.*, 2010, **20**, 3235–3243.
- 8 Y. Xia, X. He, M. Cao, C. Chen, H. Xu, F. Pan and J. R. Lu, *Biomacromolecules*, 2013, **14**, 3615–3625.
- 9 M. J. Serpe, J. Kim and L. A. Lyon, *Adv. Mater.*, 2004, **16**, 184–187.
- 10 W. Richtering, *Langmuir*, 2012, **28**, 17218–17229.
- 11 S. Wiese, A. C. Spiess and W. Richtering, *Angew. Chem., Int. Ed.*, 2012, **52**, 576–579.
- 12 V. Schmitt and V. Ravaine, *Curr. Opin. Colloid Interface Sci.*, 2013, **18**, 532–541.
- 13 S. Wellert, M. Richter, T. Hellweg, R. von Klitzing and Y. Hertle, *Z. Phys. Chem.*, 2015, **229**, 1–26.
- 14 Z. Li, D. Harbottle, E. Pensini, T. Ngai, W. Richtering and Z. Xu, *Langmuir*, 2015, **31**, 6282–6288.
- 15 O. S. Deshmukh, D. van den Ende, M. C. Stuart, F. Mugele and M. H. G. Duits, *Adv. Colloid Interface Sci.*, 2015, **222**, 215–227.
- 16 Y. Guan and Y. Zhang, *Soft Matter*, 2011, **7**, 6375.
- 17 V. Lapeyre, N. Renaudie, J.-F. Dechezelle, H. Saadaoui, S. Ravaine and V. Ravaine, *Langmuir*, 2009, **25**, 4659–4667.
- 18 J. Dubbert, T. Honold, J. S. Pedersen, A. Radulescu, M. Drechsler, M. Karg and W. Richtering, *Macromolecules*, 2014, **47**, 8700–8708.
- 19 R. Contreras-Cáceres, L. Schellkopf, C. Fernández-López, I. Pastoriza-Santos, J. Pérez-Juste and M. Stamm, *Langmuir*, 2015, **31**, 1142–1149.
- 20 K. Geisel, A. A. Rudov, I. I. Potemkin and W. Richtering, *Langmuir*, 2015, **31**, 13145–13154.
- 21 Z. Meng, M. H. Smith and L. A. Lyon, *Colloid Polym. Sci.*, 2009, **287**, 277–285.
- 22 H. Bachman, A. C. Brown, K. C. Clarke, K. S. Dhada, A. Douglas, C. E. Hansen, E. Herman, J. S. Hyatt, P. Kodekere, Z. Meng, S. Saxena, M. W. Spears Jr, N. Welsch and L. A. Lyon, *Soft Matter*, 2015, **11**, 2018–2028.
- 23 T. J. Merkel, S. W. Jones, K. P. Herlihy, F. R. Kersey, A. R. Shields and M. Napier, *et al.*, *Proc. Natl. Acad. Sci. U. S. A.*, 2011, **108**, 586–591.
- 24 S. Berger, H. Zhang and A. Pich, *Adv. Funct. Mater.*, 2009, **19**, 554–559.
- 25 G. Agrawal, A. Ülpenich, X. Zhu, M. Möller and A. Pich, *Chem. Mater.*, 2014, **26**, 5882–5891.
- 26 T. Kureha, T. Sato and D. Suzuki, *Langmuir*, 2014, **30**, 8717–8725.
- 27 L. V. Sigolaeva, S. Y. Gladyr, A. P. H. Gelissen, O. Mergel, D. V. Pergushov, I. N. Kurochkin, F. A. Plamper and W. Richtering, *Biomacromolecules*, 2014, **15**, 3735–3745.
- 28 L. V. Sigolaeva, O. Mergel, E. G. Evtushenko, S. Y. Gladyr, A. P. H. Gelissen, D. V. Pergushov, I. N. Kurochkin, F. A. Plamper and W. Richtering, *Langmuir*, 2015, **31**, 13029–13039.
- 29 M. Stieger, J. S. Pedersen, W. Richtering and P. Lindner, *J. Chem. Phys.*, 2004, **120**, 6197–6206.
- 30 S. Höfl, L. Zitzler, T. Hellweg, S. Herminghaus and F. Mugele, *Polymer*, 2007, **48**, 245–254.
- 31 O. Tagit, N. Tomeczak and G. J. Vancso, *Small*, 2008, **4**, 119–126.
- 32 S. Wellert, Y. Hertle, M. Richter, M. Medebach, D. Magerl, W. Wang, B. Demé, A. Radulescu, P. Müller-Buschbaum, T. Hellweg and R. von Klitzing, *Langmuir*, 2014, **30**, 7168–7176.
- 33 F. Schneider, A. Balaceanu, A. Feoktystov, V. Pipich, Y. Wu, J. Allgaier, W. Pyckhout-Hintzen, A. Pich and G. J. Schneider, *Langmuir*, 2014, **30**, 15317–15326.
- 34 S. Wellert, D. Kesal, S. Schön, R. von Klitzing and K. Gawlitza, *Langmuir*, 2015, **31**, 2202–2210.
- 35 J. Gao and B. J. Frisken, *Langmuir*, 2003, **19**, 5212–5216.
- 36 J. Gao and B. J. Frisken, *Langmuir*, 2003, **19**, 5217–5222.
- 37 *Neutrons, X-rays and Light: Scattering Methods Applied to Soft Condensed Matter*, ed. P. Lindner and T. Zemb, Amsterdam, North Holland Delta Series, 2002.
- 38 J. S. Pedersen, *Adv. Colloid Interface Sci.*, 1997, **70**, 171–210.
- 39 P. C. Hansen, *Discrete inverse problems: insight and algorithms*, Society for Industrial and Applied Mathematics, Philadelphia, 2010.
- 40 O. Glatter, IUCr, *J. Appl. Crystallogr.*, 1977, **10**, 415–421.
- 41 D. I. Svergun, IUCr, *J. Appl. Crystallogr.*, 1992, **25**, 495–503.
- 42 O. Glatter, *J. Appl. Crystallogr.*, 1981, **14**, 101–108.
- 43 O. Glatter and B. Hainisch, *J. Appl. Crystallogr.*, 1984, **17**, 435–441.
- 44 O. L. J. Virtanen and W. Richtering, *Colloid Polym. Sci.*, 2014, **292**, 1743–1756.
- 45 O. L. J. Virtanen, H. M. Ala-Mutka and W. Richtering, *Macromol. Chem. Phys.*, 2015, **216**, 1431–1440.
- 46 E. Jones, T. Oliphant and P. Peterson, *others*, *SciPy: Open source scientific tools for Python*, 2001.
- 47 S. van der Walt, J. L. Schonberger, J. Nunez-Iglesias, F. Boulogne, J. D. Warner, N. Yager, E. Gouillart, T. Yu and S. I. Contributors, *PeerJ*, 2014, **2**, e453.
- 48 D. Duracher, A. Elaissari and C. Pichot, *J. Polym. Sci., Part A: Polym. Chem.*, 1999, **37**, 1823–1837.
- 49 A. C. Brown, S. E. Stabenfeldt, B. Ahn, R. T. Hannan, K. S. Dhada, E. S. Herman, V. Stefanelli, N. Guzzetta, A. Alexeev, W. A. Lam, L. A. Lyon and T. H. Barker, *Nat. Mater.*, 2014, **13**, 1108–1114.
- 50 A. Mourran, Y. Wu, R. A. Gumerov, A. A. Rudov, I. I. Potemkin, A. Pich and M. Möller, *Langmuir*, 2016, **32**, 723–730.